ChemPubSoc Europe

DOI: 10.1002/chem.201904722

CHEMISTRY A European Journal Full Paper

Nanotechnology | *Very Important Paper*

3D Nitrogen-Doped Graphene Encapsulated Metallic Nickel–Iron Alloy Nanoparticles for Efficient Bifunctional Oxygen Electrocatalysis

Zhaoyang Wang[+],[a] Xiaobin Liao[+],[a] Zifeng Lin,[a] Fuzhi Huang,[a] Yalong Jiang,[a] Kwadwo Asare Owusu,[a] Lin Xu,*[a] Ziang Liu,[a] Jiantao Li,[a] Yan Zhao,[a] Yi-Bing Cheng,[a, b] and Liqiang Mai*[a]

Abstract: It is extremely desirable to explore high-efficient, affordable and robust oxygen electrocatalysts toward rechargeable Zn–air batteries (ZABs). A 3D porous nitrogen-doped graphene encapsulated metallic Ni_3Fe alloy nanoparticles aerogel (Ni_3Fe-GA_1) was constructed through a facile hydrothermal assembly and calcination process. Benefiting from 3D porous configuration with great accessibility, high electrical conductivity, abundant active sites, optimal nitrogen content and strong electronic interactions at the Ni_3Fe/N-doped graphene heterointerface, the obtained aerogel showed outstanding catalytic performance toward the oxygen evolution reaction (OER) and oxygen reduction reaction (ORR). Specifically, it exhibited an overpotential of 239 mV to attain 10 mA cm^{-2} for OER, simultaneously providing a positive onset potential of 0.93 V within a half-wave potential of 0.8 V for ORR. Accordingly, when employed in the aqueous ZABs, Ni_3Fe-GA_1 achieved higher power density and superior reversibility than Pt/C—IrO_2 catalyst, making it a potential candidate for rechargeable ZABs.

Introduction

With the increasingly serious situation of the energy crisis and environmental problems, it is tremendously urgent to develop clean and sustainable energy conversion and storage technologies, such as water-splitting devices, acidic proton exchange membrane fuel cells and rechargeable metal–air batteries.[1] Among these known energy storage applications, rechargeable Zn–air batteries (ZABs) are regarded as a promising candidate for utilization in next-generation portable electronics because of their appreciably high specific energy density (1086 Wh kg^{-1}), inexpensiveness, environmental friendliness and inherent safety.[2] However, the unsatisfied power density, low energy conversion efficiency and poor durability have greatly impeded their usage for large-scale practical applications.[3] These drawbacks of ZABs are mainly generated from the inherent sluggish kinetics of multiple electron-transfer processes in the air electrode, including the oxygen evolution and reduction reactions (OER/ORR) during the charge–discharge process.[4] Noble-metal-based electrocatalysts, such as ruthenium/iridium-based and platinum-based catalysts, are viewed as exceptional oxygen electrocatalysts.[5] Nevertheless, their scarcity, high cost, inferior durability and insufficient bifunctional catalytic activity greatly block the widespread applications.[6] With this in mind, the rational design and construction of cost-effective, highly efficient and durable oxygen electrocatalysts fabricated with earth-abundant elements is crucial.[7]

In the previous reports, 3d transition-metal (3d TMs)-based materials like nickel, iron, cobalt, copper and their alloys with nanostructures have been extensively studied as competent candidates for ZABs owing to their earth-abundance, affordability and excellent catalytic activity.[8] However, the bare 3d TMs nanomaterials are typically exposed to self-aggregation, which would bring about low specific surface areas within few catalytic active sites. Moreover, this kind of catalysts are not stable enough when measured in the harsh alkaline electrolyte.[9] It is a very effective strategy to strengthen the catalytic activities and durabilities of electrocatalysts by integrating with carbon materials, such as carbon quantum dots,[10] carbon nanotubes,[11] graphene,[12] and graphdiyne.[13] Hybridizing with high electrical conductivity of carbon materials, especially encapsulating in graphitized carbon shells, not only guarantees rapid charge transport, but also protects the highly dispersible

[a] Z. Wang,[+] X. Liao,[+] Z. Lin, Prof. F. Huang, Y. Jiang, K. A. Owusu, Prof. L. Xu, Z. Liu, Dr. J. Li, Prof. Y. Zhao, Prof. Y.-B. Cheng, Prof. L. Mai
State Key Laboratory of Advanced Technology for Materials Synthesis and Processing, State Key Laboratory of Silicate Materials for Architectures
Wuhan University of Technology, Wuhan 430070 (P. R. China)
E-mail: linxu@whut.edu.cn
mlq518@whut.edu.cn

[b] Prof. Y.-B. Cheng
ARC Centre of Excellence in Exciton Science
Monash University, Clayton, Victoria 3800 (Australia)

[+] These authors contributes equally to this work.

Supporting information and the ORCID identification number(s) for the author(s) of this article can be found under: https://doi.org/10.1002/chem.201904722.Part of a Special Issue on Electrocatalysis: Mechanism and Applications. To view the complete issue, visit Issue 18, 2020.

metallic core from corrosion by physical separation from the harsh alkaline electrolyte. More importantly, the synergistic interactions between catalysts and carbon matrix can modulate the interfacial electronic environment, as well as optimize the reaction intermediates adsorption to accelerate the catalytic kinetics.[12c,14] Cui et al. developed a universal approach to prepare several types of 3d TMs (Ni, Fe, Co and their alloys) encapsulated by single-layer graphene through a chemical vapor deposition (CVD) technique.[12a] The optimized FeNi@NC catalyst achieved the best OER catalytic activity in alkaline solution, only requiring a low overpotential of 280 mV at 10 mA cm^{-2}, as well as exhibiting superior durability. Nevertheless, the CVD method is not an economical route for large-scale production, and the unsupported metal or alloys nanoparticles can easily agglomerate during preparation.

3D nitrogen-doped graphene aerogels anchored with transition-metal nanoparticles (3D TMNP/*N*-GAs) is an effective catalyst configuration, which not only avoids self-aggregation and shedding, but also possesses rich macroporosity with easy wettability and provides multidimensional electron-transport pathways.[15] The coordination types of nitrogen dopants are mainly divided into pyridinic-N, pyrrolic-N, and graphitic-N. Among them, pyridinic-N and graphitic-N are considered as active sites for the ORR and OER.[6a,16] In the previous theoretical calculation results, active sites in the graphene model with higher nitrogen content are easily poisoned due to higher affinity for adsorbed oxygen.[17] Therefore, it is very important to rationally design and construct the 3D TMNP/*N*-GAs with suitable nitrogen content for the development of bifunctional 3d TM electrocatalysts toward rechargeable ZAB. Meanwhile, the synergistic catalytic mechanism between metal and N-doped graphene is still ambiguous.

Herein, we report the metallic Ni_3Fe alloy nanoparticles encapsulated in 3D porous N-doped graphene aerogel (Ni_3Fe-GA_1) with appropriate nitrogen content synthesized by a facile hydrothermal assembly and subsequent calcination. The prepared Ni_3Fe-GA_1 hybrid catalyst exhibited outstanding OER and ORR catalytic performance. The reason for this electrocatalytic behavior could be attributed to a 3D porous configuration with great accessibility, high electrical conductivity, abundant active sites, optimal nitrogen content, and regulation of charge distribution in the Ni_3Fe alloy/N-doped graphene interface. Calculations using DFT verified that the Ni_3Fe/N-doped graphene models delivered stronger interfacial coupling induced by the nitrogen dopants than that of the Ni_3Fe/graphene model, as well as obviously diminishing the electron density localization around the metal atoms. Simultaneously, the d-band center shifts downwards relative to Fermi level after coordinating with graphene. This probably optimized the surface active centers and synergistically facilitated the adsorption/desorption of oxygen intermediates to accelerate the OER/ORR kinetics. Impressively, as bifunctional air cathode catalyst in rechargeable ZAB system, Ni_3Fe-GA_1 exhibited higher power density and superior reversibility than the Pt/C–IrO_2 catalyst.

Results and Discussion

As illustrated in Scheme 1, Ni_3Fe-GAs were prepared by a facile hydrothermal assembly of NiFe layer double hydroxide (NiFe-LDH) nanosheets and pyrrole monomer onto 3D GAs support followed by a calcination process. In a typical experiment, NiFe-LDH nanosheets were first synthesized by a simple hydrothermal method. Subsequently, the NiFe-LDH and a certain amount of pyrrole monomer were ultrasonically mixed with graphene oxide (GO) aqueous solution. Then, rGO/NiFe-LDH/Py aerogel was constructed through a self-assembly hydrothermal method, followed by a vacuum freeze-drying process. Finally, Ni_3Fe-GAs with various nitrogen content were obtained after a thermal treatment at 700 °C in NH_3 or H_2/Ar atmosphere. As shown in Figure S1, Supporting Information, rGO/NiFe-LDH/Py aerogel possessed twice the volume of rGO/NiFe-LDH aerogel. XRD patterns (Figure S2A–B, Supporting Information) and SEM images (Figure S3, Supporting Information) confirmed that NiFe-LDH nanosheets with an average size of 150 nm were successfully assembled on the 3D graphene framework. The HR-XPS) spectrum of Ni 2p and Fe 2p indicated the Ni^{2+} and Fe^{3+} states in NiFe-LDH (Figure S4, Supporting Information). In the FTIR spectra (Figure S2C) of rGO/NiFe-LDH/Py aerogel and GA, the peaks located at 1562 and 1354 cm^{-1} were attributed to the stretching vibrations of pyrrole rings and C–N stretching

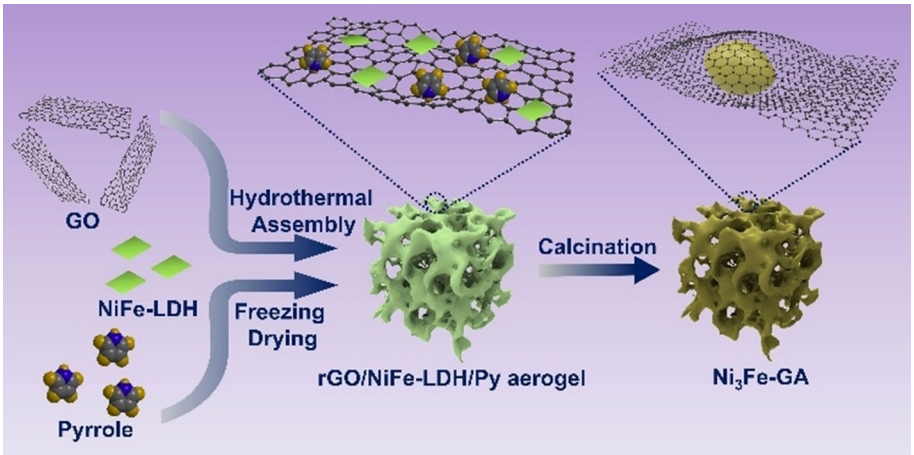

Scheme 1. Illustration of the preparation of Ni_3Fe-GA samples.

vibrations, respectively.[18] In addition, the peak located below 1000 cm^{-1}, such as 617 and 519 cm^{-1}, could be ascribed to the classical M–O stretching and bending vibrations of hydrotalcite and further confirmed the existence of NiFe-LDH in the rGO/NiFe-LDH/Py aerogel.[19] These results revealed that the pyrrole was decorated on the surface of graphene support, which could effectively suppress the self-stacking behavior of GO during the self-assembly processes.[18b,20] Accordingly, the 3D graphene architecture with modified pyrrole exhibited thinner connection walls and a more open porous network with continuous macropores.

The XRD pattern of the prepared Ni_3Fe-GA_1 sample is shown in Figure 1 A. As observed, the diffraction peaks at 44.1, 51.4, and 75.5° can be assigned to the (111), (200) and (220) lattice planes of Ni_3Fe (JCPDS No. 03-065-3244), respectively. The weak peak at about 26° in 2θ originates from the (002) graphitic diffraction of graphene. Based on TGA (Figure S5A, Supporting Information) in air, the content of Ni_3Fe in Ni_3Fe-GA_1 is calculated to be 46 wt.%. From the N_2 adsorption–desorption analysis in Figure S5B, Ni_3Fe-GA_1 presents a high Brunauer–Emmett–Teller (BET) specific surface area of 151.8 $m^2 g^{-1}$. SEM images (Figure 1 B,C) show that the unique interconnected 3D hierarchical structure with continuous macropores and thin connection walls can be retained after annealing, which can expose more active surface, favor charge/mass transport and enhance the electrolyte accessibility. Obviously, the TEM images (Figure 1 D,E) display that the sizes of the Ni_3Fe alloy nanoparticles encapsulated in *N*-graphene sheets are distributed at 15–30 nm. The selected area electron diffraction (SAED) pattern clearly presents diffraction rings in Figure 1 F, which can be indexed to polycrystalline Ni_3Fe and *N*-graphene matrix. The HR-TEM images (Figure 1 G) exhibit the fringe spacing of 0.177 and 0.204 nm, corresponding to the (200) and (111) crystal plane of Ni_3Fe, respectively. In addition, it also illustrates that the *N*-graphene layers encapsulated Ni_3Fe alloy nanoparticles are in the range of 3 to 5 layers. The high angle annular dark field (HAADF) image and corresponding element mapping analysis are given in Figure 1 H, which obviously reveal uniform distributions of Ni and Fe elements with an atomic ratio of 2.7:1 in the alloy particles. Meanwhile, it also verifies that N element is homogeneously dispersed throughout the graphene sheets, derived from pyrrole and NH_3 as nitrogen sources.

For comparison, Ni_3Fe-GA_2, Ni_3Fe-GA_3, and Ni_3Fe-GA_4 samples were also prepared through a similar annealing treatment in NH_3 or H_2/Ar atmosphere. Their XRD patterns, SEM, and TEM images are provided in Figures S6 and S7. Obviously, the average sizes of Ni_3Fe nanoparticles calcined in NH_3 are smaller than those calcined in H_2/Ar. The chemical composition, surface valence state and interfacial interaction were further conducted by XPS analysis. The XPS full spectrum in Figure 2 A confirms the existence of Ni, Fe, C and N elements in the Ni_3Fe-GA samples. Ni_3Fe-GA_1 exhibits a N/C ratio of 6.40 at%,

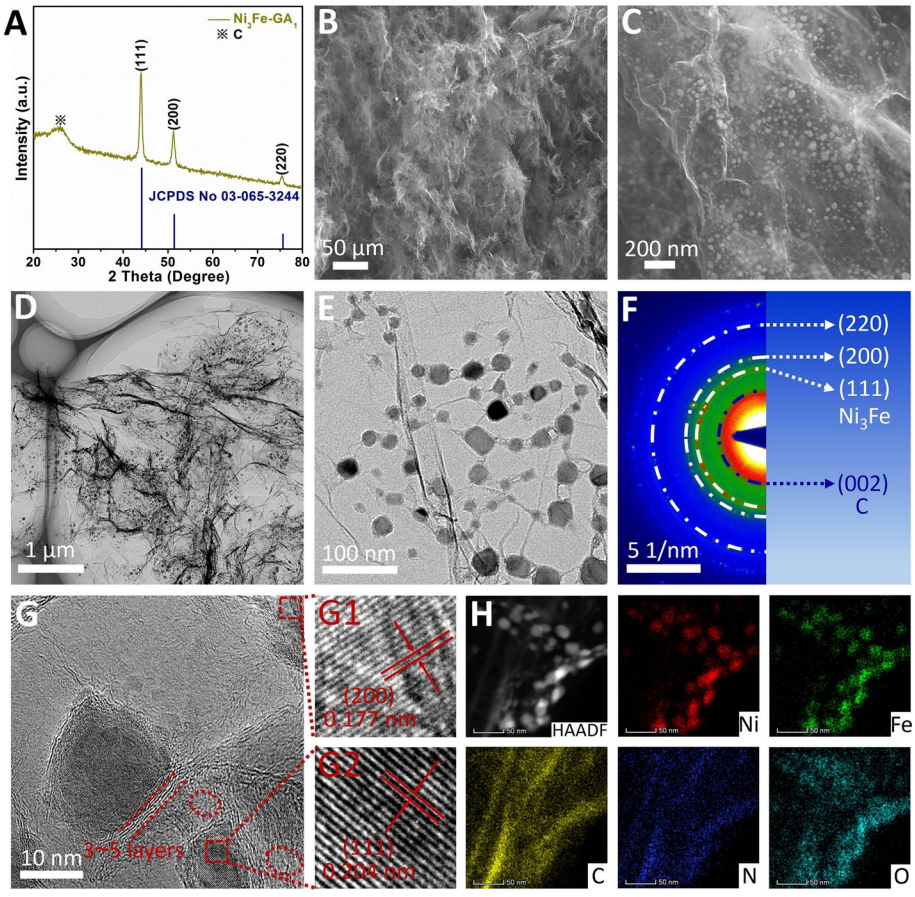

Figure 1. (A) XRD pattern for Ni_3Fe-GA_1 sample. (B,C) SEM images. (D,E) TEM images. (F) SAED pattern. (G) HRTEM image. (H) STEM image and corresponding elemental mapping.

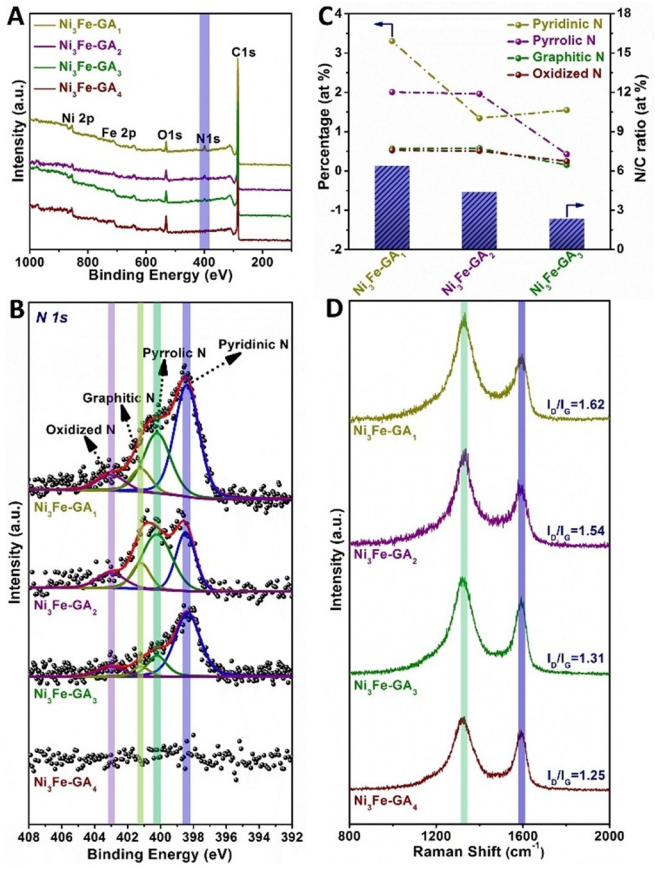

Figure 2. XPS spectrum (A), high-resolution XPS N 1s spectra (B) and Raman spectra (D) of Ni_3Fe-GA_1, Ni_3Fe-GA_2, Ni_3Fe-GA_3, and Ni_3Fe-GA_4. Percentage of various nitrogen species among different simples (C).

which is higher than that of Ni_3Fe-GA_2 (4.39 at%), Ni_3Fe-GA_3 (2.37 at%), and Ni_3Fe-GA_4 (0 at%). It can be simplified into four peaks in the HR N 1 s spectrum (Figure 2B), namely pyridinic N, pyrrolic N, graphitic N, and oxidized N with binding energies of 398.4, 400.2, 401.2, and 403.0 eV, respectively.[6a,21] Moreover, the percentages of various nitrogen species are provided in Figure 2C. It is obvious that the total nitrogen content and concentration of pyrrolic-N are apparently improved via decorating pyrrole on the surface of graphene followed by pyrolysis. Simultaneously, compared with that of Ni_3Fe-GA_2 after H_2/Ar pyrolysis, the concentration of pyridinic-N in Ni_3Fe-GA_1 increases from 1.34 to 3.30 at%, while the percentage of pyrrolic-N decreases from 44.7 to 31.4%, demonstrating a transformation from pyrrolic-N to pyridinic-N during NH_3 annealing process. These results reveal that the proportion of various specific nitrogen species in Ni_3Fe-GA samples, especially for pyridinic-N, can be optimized by adopting suitable pyrolysis atmosphere and modification with pyrrole. According to previous studies, it has been known that pyridinic-N species can be conducted as active sites for OER and ORR.[16a,22] As for the HR spectrum of C 1s in Figure S8A, Supporting Information, it can be fitted into three peaks at about 284.6, 285.4, and 286.3 eV, which are derived from C–C, C–N, and C=O species, respectively.[11c,14a,15c] The observation of C–N bonding further confirms the formation of nitrogen-doped carbon. The O 1s spectrum in Figure S8B reveals the presence of metal–O (529.8 eV), O=C (531.4 eV), and C–OH (533.4 eV). As shown in Figure 2D, the Raman spectrum of Ni3Fe-GA samples show two prominent peaks at 1330 and 1590 cm^{-1}, corresponding to the disordered carbon (D-band) and graphitic carbon (G-band), respectively. Furthermore, the intensity ratios of D and G-bands (I_D/I_G) are calculated and they exhibit a decreasing trend in the order of Ni_3Fe-GA_1 (1.62) > Ni_3Fe-GA_2 (1.54) > Ni_3Fe-GA_3 (1.31) > Ni_3Fe-GA_4 (1.25). This result indicates that more defects on the surface of graphene are generated by modifying pyrrole followed by NH_3 pyrolysis along with the increase of nitrogen content, which can contribute to the reinforced electrocatalytic activity.[23]

As shown in Figure S9A, the peaks located at 852.9, 855.4, 861.2, 870.5, 873.4, and 879.6 eV in the high-resolution XPS spectra of Ni 2p can be assigned to the metallic Ni, oxidized Ni species and satellite peaks, respectively.[14a] Similarly, for the Fe 2p spectra (Figure S9B, Supporting Information), the peaks located at 707.3 and 719.5 eV are ascribed to Fe $2p_{3/2}$ and Fe $2p_{1/2}$, respectively, corresponding to metallic Fe.[14a] The binding energy centered at 711.7 and 724.6 eV are attributed to oxidation state of Fe species (Fe^{3+}). The peaks at 715.6 and 729.6 eV can be attributed to satellite peaks. The oxidized Ni and Fe species reveal that the surfaces can be partially oxidized when Ni_3Fe nanoparticles are exposed in the air, which is similar to the previous results on alloys. It is worth noting that the binding energies of both Ni and Fe in Ni_3Fe-GA_1 deliver a positive shift of 0.3 and 0.5 eV, compared with that of Ni_3Fe, respectively. The shifts of Ni and Fe binding energy indicate the existence of strong electronic interactions between Ni_3Fe and N-doped graphene. To further understand the interfacial charge behavior of the Ni_3Fe/N-doped graphene interface, DFT was performed to calculate the charge density of four models, including Ni_3Fe/Pyridinic *N*-Graphene, Ni_3Fe/Pyrrolic *N*-Graphene, Ni_3Fe/Graphitic *N*-Graphene, and Ni_3Fe/Graphene models. The electronic density of states of Ni_3Fe/*N*-Graphene models indicate the metallic nature with strengthened carrier densities near the Fermi level than that of Ni_3Fe (Figure S10, Supporting Information). As confirmed from the comparison of charge density differences in Figure 3, after nitrogen doping in graphene, stronger charge redistribution and polarization occur at the interface region, significantly increasing the electronic distribution asymmetry degree.[24] Meanwhile, the sliced electron localization function (ELF) analysis exhibit that the electron density localization around the metal atoms adjacent to N-doped graphene can be decreased by the difference of the electronegativity between C (2.55) and N (3.04), compared with that of Ni_3Fe/Graphene model. Notably, the d-band center of Ni_3Fe, Ni_3Fe/Pyridinic *N*-Graphene, Ni_3Fe/Pyrrolic *N*-Graphene, Ni_3Fe/Graphitic *N*-Graphene, and Ni_3Fe/Graphene models are calculated to be −2.03, −2.28, −2.18, −2.15, and −2.21 eV, respectively, suggesting the d-band positions shift downwards relative to the Fermi level after coordinating with graphene (Figure S11, Supporting Information). According to the d-band theory, the metal–O bonding strength is decreased due to the lower antibonding energy states, facilitating the desorption of adsorbates.[25] The above-mentioned results verified the strong

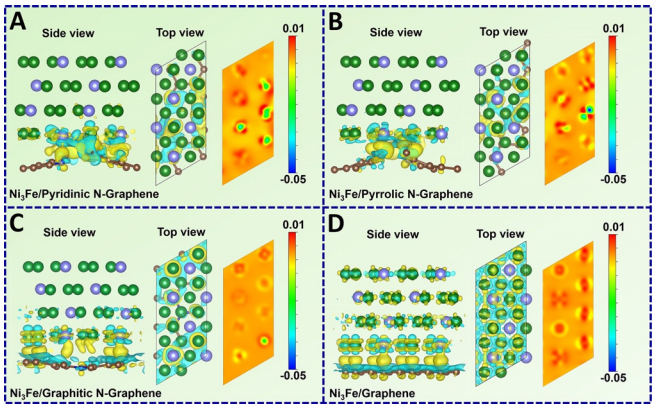

Figure 3. Side and top view for the isosurfaces of local charge density difference of Ni_3Fe/Pyridinic *N*-Graphene (A), Ni_3Fe/Pyrrolic *N*-Graphene (B), Ni_3Fe/Graphitic *N*-Graphene (C), and Ni_3Fe/Graphene models (D) as well as corresponding sliced ELF of the Ni_3Fe monolayer. The atoms in green, purple, brown, and blue represent Ni, Fe, C, and N, respectively. Yellow and cyan regions represent electron accumulation and depletion, respectively.

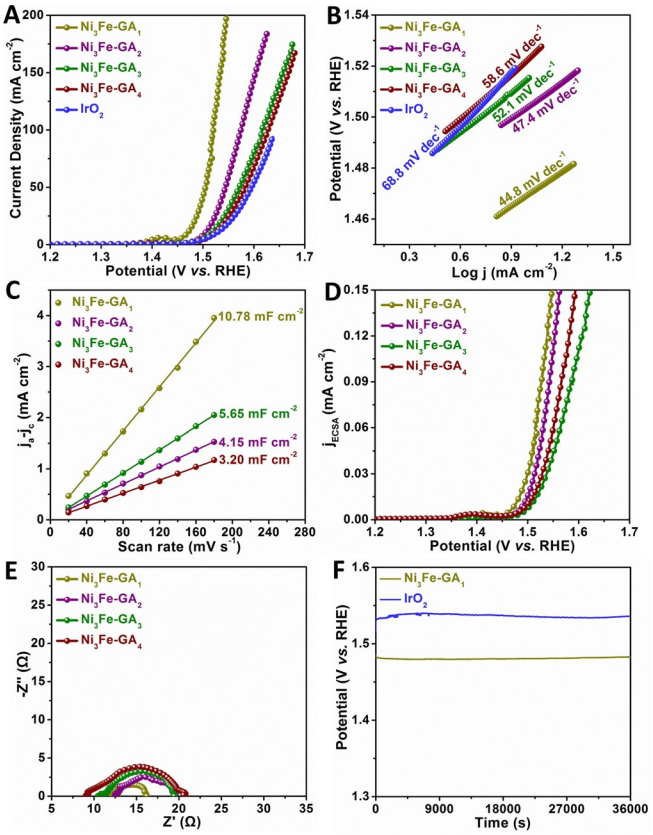

Figure 4. (A) OER polarization curves and (B) corresponding Tafel plots for Ni_3Fe-GA_1, Ni_3Fe-GA_2, Ni_3Fe-GA_3, Ni_3Fe-GA_4, and IrO_2 catalysts in O_2-saturated 1.0 M KOH solution. (C) Current difference (j_{anodic}—$j_{cathodic}$) plotted against scan rate. (D) Polarization curves normalized by the electrochemically active surface area (ECSA). (E) Nyquist plots measured at 1.54 V vs. RHE. (F) Chronopotentiometric curves of Ni_3Fe-GA_1 and IrO_2 catalysts at the current densities of 10 mA cm^{-2}.

electronic interactions at the Ni_3Fe/N-doped graphene heterointerface, which can induce the redistribution of charge on the interface, modulate the electronic structure of catalyst surface, tailor the d band center relative to Fermi level, and optimize the adsorption energy of reaction intermediates to accelerate the catalytic kinetics.[25]

The OER performances of the prepared Ni_3Fe-GA_1, Ni_3Fe-GA_2, Ni_3Fe-GA_3, Ni_3Fe-GA_4, and IrO_2 catalysts are measured by a three-electrode system in O_2-saturated 1.0 M KOH electrolyte. Figure 4A and Figure S12A, Supporting Information, present the linear sweep voltammetry (LSV) curves with iR-compensation at a sweep rate of 5 mV s^{-1} recorded by rotating disk electrode at 1600 rpm. As a contrast, the LSV curves without iR-compensation are shown in Figure S13, Supporting Information. Ni_3Fe-GA_1 requires an overpotential of only 239 mV to reach a current density of 10 mA cm^{-2}, which is lower than that of Ni_3Fe-GA_2 (274 mV), Ni_3Fe-GA_3 (284 mV), Ni_3Fe-GA_4 (293 mV), Ni_3Fe (313 mV), and IrO_2 (297 mV). Meanwhile, the Tafel plots in Figure 4B and Figure S12B, Supporting Information, can be obtained by fitting the corresponding LSV curves. Ni_3Fe-GA_1 possesses the lowest Tafel slope of 44.8 mV dec^{-1}, indicating its fast catalytic rate and favorable OER kinetics. Furthermore, electrochemically active surface area (ECSA) was evaluated by the double layer capacitance (C_{dl}) determined from cyclic voltammetry (CV) plots in the non-Faradaic potential window. As illustrated in Figure 4C and Figures S12D and S14, Supporting Information, the C_{dl} of Ni_3Fe-GA_1 was calculated to be 10.78 mF cm^{-2}, which is much higher than that of Ni_3Fe-GA_2 (4.15 mF cm^{-2}), Ni_3Fe-GA_3 (5.65 mF cm^{-2}), Ni_3Fe-GA_4 (3.20 mF cm^{-2}), and Ni_3Fe (1.35 mF cm^{-2}), demonstrating the higher active surface area. The ECSA-normalized LSV plots are displayed in Figure 4D and Figure S12F, Supporting Information, which are utilized to highlight the intrinsic catalytic activity.[26] It is clear that Ni_3Fe-GA_1 with ECSA-normalized delivers the best intrinsic catalytic activity compared with other samples, suggesting the enhancement in activity originates not only from the improvement of active surface area but also the introduction of moderate nitrogen content, which can intrinsically optimize the interfacial catalytic behaviors. Figure S15, Supporting Information, presents the OER activities of Ni_3Fe/GA synthesized with different volume (0, 10, 20, 30, 100, and 1000 μL) of pyrrole in NH_3 pyrolysis. It is obvious that Ni_3Fe-GA using 20 μL of pyrrole delivers the best catalytic performance. The nitrogen-doped content can be raised by increasing the pyrrole mass. However, excessively high nitrogen content will lower the electrical conductivity of graphene, decreasing the catalytic activity.[27] Electrochemical impedance spectroscopy (EIS) was conducted to investigate the charge transfer kinetics during the OER process. As shown in Figure 4E, Ni_3Fe-GA_1 exhibits the smallest charge-transfer resistance (R_{ct}) among the samples, indicating more desirable electron-transport and faster reaction kinetics for OER catalysis. The catalytic stability which is also an important factor for evaluating an outstanding electrocatalyst was appraised by chronoamperometry measurement. The lower overpotential of Ni_3Fe-GA_1 compared with IrO_2 in Figure 4F can be maintained for 36000 s. Meanwhile, the morphology and element distribution are retained well after OER stability (Figure S17, Supporting Information). All the results reveal the excellent OER durability of Ni_3Fe-GA_1 sample.

In addition to the outstanding OER performance discussed above, we also investigated the ORR activity of synthesized samples using the rotating disc electrode (RDE) measurements in O_2-saturated 0.1 M KOH solution. As shown in Figure 5A and Figure S18A, Supporting Information, Ni_3Fe-GA_1 displays the high onset potential (E_{onset}) and corresponding half-wave potential ($E_{1/2}$) of 0.93 and 0.80 V versus RHE, respectively. These values are very close to those of commercial Pt/C catalyst (0.98 and 0.83 V), but obviously better than those of Ni_3Fe-GA_2 (0.83 and 0.74 V), Ni_3Fe-GA_3 (0.86 and 0.75 V), Ni_3Fe-GA_4 (0.81 and 0.69 V), and Ni_3Fe (0.77 and 0.54 V), highlighting the superior ORR activity of Ni_3Fe-GA_1. Figure S18B exhibits the ORR activities of Ni_3Fe-GA prepared with different volumes (0, 10, 20, 30,100, and 1000 μL) of pyrrole followed by NH_3 pyrolysis, suggesting the best catalytic performance of Ni_3Fe-GA is achieved using 20 μL of pyrrole. To evaluate the electron-transfer kinetics of synthesized catalysts, the polarization curves were tested at the various rotating speeds from 400 to 1600 rpm, simultaneously constructing the corresponding Koutecky–Levich (K–L) plots. As presented in Figure 5C, Ni_3Fe-GA_1 displays well-defined plateau of diffusion-limited currents at various rotating speeds. The average electron-transfer number (n) of Ni_3Fe-GA_1 is about 3.5 at potentials from 0.30 to 0.45 V calculated from the K–L plots (Figure S19B, Supporting Information), which is higher than that of Ni_3Fe-GA_2 (2.9), Ni_3Fe-GA_3 (2.8), Ni_3Fe-GA_4 (2.4), and Ni_3Fe (3.2), respectively, indicating the superior ORR activity through a close four-electron transfer process. To further clarify the ORR pathway, the rotating ring-disk electrode (RRDE) measurements were performed at 1600 rpm. The disk current density corresponds to ORR process and the ring current density determines the hydrogen peroxide species. As shown in Figures 5D,E, for Ni_3Fe-GA_1 catalyst, the calculated n is around 3.85 and H_2O_2 yield is below 10% at 0.6–0.8 V, which are very close to those of the Pt/C catalyst, suggesting its four-electron-dominated ORR pathway. Furthermore, the ORR stability can be evaluated by chronoamperometric measurements performed at the half-wave potentials of catalysts with 1600 rpm. After continuous operation for 20000 s, Ni_3Fe-GA_1 maintains 78% of its initial current density, while only 61% of the original current density was retained by the Pt/C.

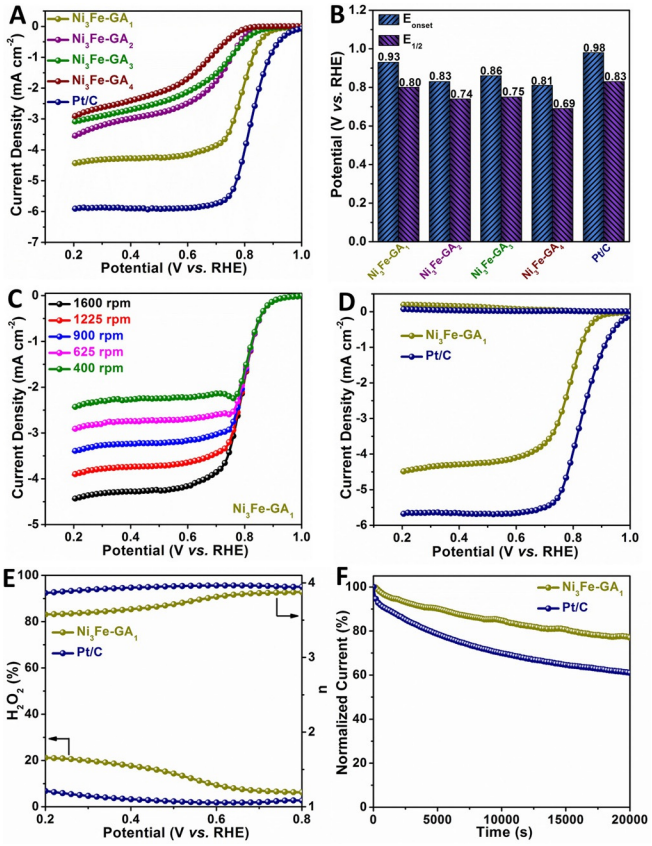

Figure 5. (A) ORR polarization curves for Ni_3Fe-GA_1, Ni_3Fe-GA_2, Ni_3Fe-GA_3, Ni_3Fe-GA_4 and Pt/C catalysts in O_2-saturated 0.1 M KOH solution. (B) Bar plots of onset potentials (E_{onset}) and half-wave potentials ($E_{1/2}$). (C) LSV curves of Ni_3Fe-GA_1 catalyst tested with different rotating speeds in rpm. (D) RRDE measurements for Ni_3Fe-GA_1 and Pt/C catalysts at 1600 rpm. (E) The H_2O_2 yield and electron-transfer number calculated based on the corresponding RRDE data. (F) ORR chronoamperometric response of Ni_3Fe-GA_1 and Pt/C catalysts.

The overall activity of bifunctional oxygen catalyst can be evaluated by the potential difference (ΔE) between the $E_{1/2}$ of ORR and E_{j10} of OER ($\Delta E = E_{j10} - E_{1/2}$).[4b,7c,Sb] As shown in Figure S24, Supporting Information, Ni_3Fe-GA_1 exhibits a considerably smaller ΔE of 0.74 V than the Pt/C & IrO_2 mixture catalyst (0.87 V), indicating superior catalytic bifunctionality. As summarized in Table S1, Supporting Information, the potential difference presented here is superior than those of recently reported state-of-the-art bifunctional non-noble metal electrocatalysts. The excellent OER and ORR catalytic activity makes Ni_3Fe-GA_1 a promising candidate as the oxygen catalyst in air electrode for rechargeable ZAB. To evaluate the practical applicability, as illustrated in Figure 6A, we constructed a ZAB in two-electrode configuration using Ni_3Fe-GA_1 or benchmark mixture catalyst of Pt/C & IrO_2 loaded onto a carbon cloth as the air cathode, a Zn plate as the anode, and 6.0 M KOH with 0.2 M $Zn(CH_3COO)_2$ as the electrolyte. The open-circuit voltage of the ZAB employing Ni_3Fe-GA_1 as air electrode catalyst is 1.44 V (Figure 6B). The discharge polarization curves and corresponding power density curves are given in Figure 6C. The maximum power density of the ZAB equipped with Ni_3Fe-GA_1 catalyst is calculated to be 62.9 mW cm^{-2}, which is higher than that with Pt/C & IrO_2 mixture catalyst (49.6 mW cm^{-2}). Furthermore, the specific capacity of ZAB based on Ni_3Fe-GA_1 catalyst is 756 mAh g_{Zn}^{-1} at 10 mA cm^{-2} corresponding to a large energy density of 845 Wh kg^{-1} (Figure 6D), which is superior than those of Pt/C & IrO_2 (719 mAh g_{Zn}^{-1}; 826 Wh kg^{-1}). ZAB was measured by galvanostatic charging and discharging at 10 mA cm^{-2} with each cycle spanning 20 min to evaluate the battery rechargeability (Figure 6E). The ZAB assembled with Ni_3Fe-GA_1 presents an excellent cycling performance over 100 h (300 cycles) with a small overpotential increase in comparison to that of the Pt/C & IrO_2 mixture catalyst.

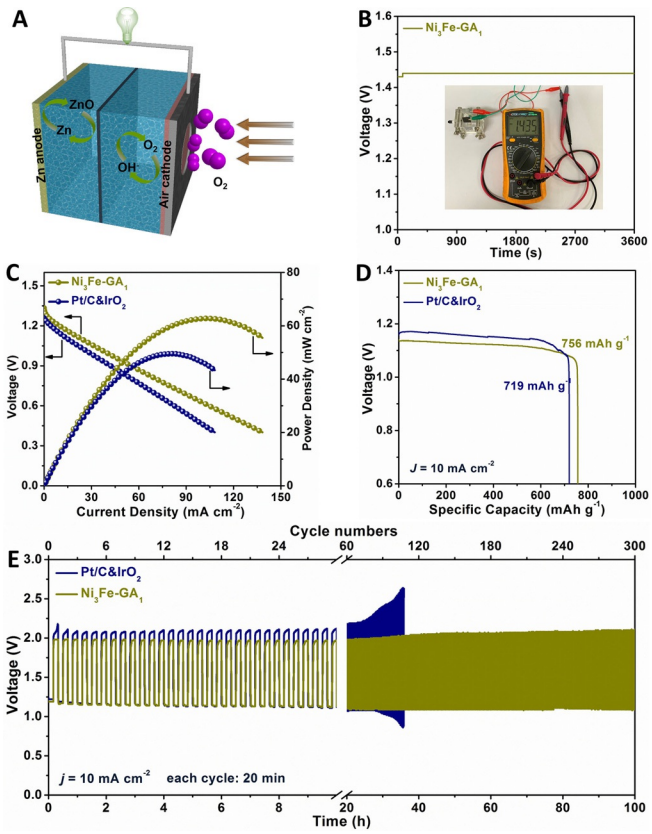

Figure 6. (A) A schematic illustration of the ZAB configuration. (B) Open-circuit plot and photograph of the ZAB using Ni_3Fe-GA_1 catalyst. (C) Comparison of the discharge polarization and power density curves using Ni_3Fe-GA_1 and Pt/C & IrO_2 as catalysts. (D) Typical discharge curves of Ni_3Fe-GA_1 and Pt/C & IrO_2 based ZABs at 10 mA cm^{-2}. (E) Galvanostatic charge and discharge cycling curves of Ni_3Fe-GA_1 and Pt/C & IrO_2 based ZABs at a current density of 10 mA cm^{-2}.

Conclusions

In conclusion, we have successfully constructed a unique bifunctional oxygen catalyst of metallic Ni_3Fe nanoparticles decorated on 3D porous N-doped graphene aerogel. Optimal nitrogen content can be obtained by modulating pyrrole volume and adopting suitable pyrolysis atmosphere. Compared to commercial IrO_2 and Pt/C electrocatalysts, the Ni_3Fe-GA_1 hybrid exhibits outstanding activity and stability for both OER and ORR. The remarkable catalytic performance can be attributed to the following advantages. 1) The interconnected 3D hierarchical structure with continuous macropores can expose more active surface, enhance the electrolyte accessibility and provide multidimensional electron transport pathways.[15b,c,28] 2) Modifying pyrrole followed by NH_3 pyrolysis results in more defects and high nitrogen content in graphene, providing much catalytic active sites.[23] 3) Theoretical calculations suggested the strong electronic interactions between Ni_3Fe and N-doped graphene, which can induce the redistribution of charge on the interface and modulate the electronic structure. The d band center shifts downwards relative to Fermi level after cooperating with graphene, probably optimizing the adsorption energy of reaction intermediates to accelerate the catalytic kinetics.[25a,29] Furthermore, as bifunctional air cathode catalyst in rechargeable ZAB system, Ni_3Fe-GA_1 exhibited higher power density and superior reversibility than Pt/C-IrO_2 catalyst. This work will provide a new insight for rationally designing and constructing efficient non- noble metal-based bifunctional electrocatalysts through interfacial regulation for renewable energy storage and conversion.

Acknowledgements

Z.W. and X.L. contributed equally to this work. This work was supported by the National Natural Science Fund for Distinguished Young Scholars (51425204), the National Natural Science Foundation of China (51521001), the National Key Research and Development Program of China (2016YFA0202603), the Programme of Introducing Talents of Discipline to Universities (B17034), the Fundamental Research Funds for the Central Universities (WUT: 2018IVA091, 2019IVB054, 2019III062JL, 2019-zy-048).

Conflict of interest

The authors declare no conflict of interest.

Keywords: 3D nitrogen-doped graphene aerogel · bifunctional electrocatalyst · interface engineering · nanoparticles · Zn–air batteries

[1] a) B. You, Y. Sun, *Acc. Chem. Res.* **2018**, *51*, 1571 – 1580; b) M. K. Debe, *Nature* **2012**, *486*, 43; c) J. S. Lee, S. T. Kim, R. Cao, N. S. Choi, M. Liu, K. T. Lee, J. Cho, *Adv. Energy Mater.* **2011**, *1*, 34 – 50.

[2] a) Y. Li, M. Gong, Y. Liang, J. Feng, J.-E. Kim, H. Wang, G. Hong, B. Zhang, H. Dai, *Nat. Commun.* **2013**, *4*, 1805; b) J. Zhang, Z. Zhao, Z. Xia, L. Dai, *Nat. Nanotechnol.* **2015**, *10*, 444 – 452.

[3] a) Y. Jiao, Y. Zheng, M. Jaroniec, S. Z. Qiao, *Chem. Soc. Rev.* **2015**, *44*, 2060 – 2086; b) M. Wu, G. Zhang, M. Wu, J. Prakash, S. Sun, *Energy Storage Mater.* **2019**, *21*, 253 – 286.

[4] a) B. Q. Li, C. X. Zhao, S. Chen, J. N. Liu, X. Chen, L. Song, Q. Zhang, *Adv. Mater.* **2019**, *31*, 1900592; b) Z. Zhang, Y.-P. Deng, Z. Xing, D. Luo, S. Sy, Z. P. Cano, G. Liu, Y. Jiang, Z. Chen, *ACS Nano* **2019**, *13*, 7062 – 7072.

[5] a) C. C. McCrory, S. Jung, J. C. Peters, T. F. Jaramillo, *J. Am. Chem. Soc.* **2013**, *135*, 16977 – 16987; b) X. Wang, Z. Li, Y. Qu, T. Yuan, W. Wang, Y. Wu, Y. Li, *Chem* **2019**, *5*, 1486 – 1511.

[6] a) H. B. Yang, J. Miao, S.-F. Hung, J. Chen, H. B. Tao, X. Wang, L. Zhang, R. Chen, J. Gao, H. M. Chen, L. Dai, B. Liu, *Sci. Adv.* **2016**, *2*, e1501122; b) C. Guo, Y. Zheng, J. Ran, F. Xie, M. Jaroniec, S. Z. Qiao, *Angew. Chem. Int. Ed.* **2017**, *56*, 8539 – 8543; *Angew. Chem.* **2017**, *129*, 8659 – 8663.

[7] a) Y. Jiang, Y. P. Deng, J. Fu, D. U. Lee, R. Liang, Z. P. Cano, Y. Liu, Z. Bai, S. Hwang, L. Yang, D. Su, W. Chu, Z. Chen, *Adv. Energy Mater.* **2018**, *8*, 1702900; b) I. S. Amiinu, X. Liu, Z. Pu, W. Li, Q. Li, J. Zhang, H. Tang, H. Zhang, S. Mu, *Adv. Funct. Mater.* **2018**, *28*, 1704638; c) Y. Qiao, P. Yuan, Y. Hu, J. Zhang, S. Mu, J. Zhou, H. Li, H. Xia, J. He, Q. Xu, *Adv. Mater.* **2018**, *30*, 1804504; d) S. S. Shinde, C. H. Lee, J.-Y. Jung, N. K. Wagh, S.-H. Kim, D.-H. Kim, C. Lin, S. U. Lee, J.-H. Lee, *Energy Environ. Sci.* **2019**, *12*, 727 – 738; e) G. Liu, J. Li, J. Fu, G. Jiang, G. Lui, D. Luo, Y. P. Deng, J. Zhang, Z. P. Cano, A. Yu, D. Su, Z. Bai, L. Yang, Z. Chen, *Adv. Mater.* **2019**, *31*, 1806761; f) P. Yu, L. Wang, Y. Xie, C. Tian, F. Sun, J. Ma, M. Tong, W. Zhou, J. Li, H. Fu, *Small* **2018**, *14*, 1801717.

[8] a) W. C. Ellis, N. D. McDaniel, S. Bernhard, T. J. Collins, *J. Am. Chem. Soc.* **2010**, *132*, 10990 – 10991; b) S. Fu, J. Song, C. Zhu, G.-L. Xu, K. Amine, C. Sun, X. Li, M. H. Engelhard, D. Du, Y. Lin, *Nano Energy* **2018**, *44*, 319 – 326; c) L. Fan, P. Zhang, B. Zhang, Q. Daniel, B. J. Timmer, F. Zhang, L.

Sun, *ACS Energy Lett.* **2018**, *3*, 2865 – 2874; d) Q. Sun, Y. Dong, Z. Wang, S. Yin, C. Zhao, *Small* **2018**, *14*, 1704137; e) P. Yu, L. Wang, F. Sun, Y. Xie, X. Liu, J. Ma, X. Wang, C. Tian, J. Li, H. Fu, *Adv. Mater.* **2019**, *31*, 1901666; f) Z. Du, P. Yu, L. Wang, C. Tian, X. Liu, G. Zhang, H. Fu, *Sci. China Mater.* **2019**, DOI: https://doi.org/10.1007/s40843-019-1190-3; g) Q. Liu, L. Wang, X. Liu, P. Yu, C. Tian, H. Fu, *Sci. China Mater.* **2019**, *62*, 624 – 632.

[9] a) T. Zhou, W. Xu, N. Zhang, Z. Du, C. Zhong, W. Yan, H. Ju, W. Chu, H. Jiang, C. Wu, Y. Xie, *Adv. Mater.* **2019**, *31*, 1807468; b) M. Gong, W. Zhou, M. J. Kenney, R. Kapusta, S. Cowley, Y. Wu, B. Lu, M. C. Lin, D. Y. Wang, J. Yang, B.-J. Hwang, H. Dai, *Angew. Chem. Int. Ed.* **2015**, *54*, 11989 – 11993; *Angew. Chem.* **2015**, *127*, 12157 – 12161.

[10] a) W. Li, Y. Liu, M. Wu, X. Feng, S. A. Redfern, Y. Shang, X. Yong, T. Feng, K. Wu, Z. Liu, *Adv. Mater.* **2018**, *30*, 1800676; b) M. Zhou, Q. Weng, Z. I. Popov, Y. Yang, L. Y. Antipina, P. B. Sorokin, X. Wang, Y. Bando, D. Golberg, *ACS Nano* **2018**, *12*, 4148 – 4155.

[11] a) C. Y. Su, H. Cheng, W. Li, Z. Q. Liu, N. Li, Z. Hou, F. Q. Bai, H. X. Zhang, T. Y. Ma, *Adv. Energy Mater.* **2017**, *7*, 1602420; b) X. Liu, L. Wang, P. Yu, C. Tian, F. Sun, J. Ma, W. Li, H. Fu, *Angew. Chem.* **2018**, *130*, 16398 – 16402; c) Z. Yang, C. Zhao, Y. Qu, H. Zhou, F. Zhou, J. Wang, Y. Wu, Y. Li, *Adv. Mater.* **2019**, *31*, 1808043.

[12] a) X. Cui, P. Ren, D. Deng, J. Deng, X. Bao, *Energy Environ. Sci.* **2016**, *9*, 123 – 129; b) G. Fu, Z. Cui, Y. Chen, Y. Li, Y. Tang, J. B. Goodenough, *Adv. Energy Mater.* **2017**, *7*, 1601172; c) Y. Yang, Z. Lin, S. Gao, J. Su, Z. Lun, G. Xia, J. Chen, R. Zhang, Q. Chen, *ACS Catal.* **2017**, *7*, 469 – 479; d) J. Fu, F. M. Hassan, C. Zhong, J. Lu, H. Liu, A. Yu, Z. Chen, *Adv. Mater.* **2017**, *29*, 1702526.

[13] a) L. Hui, Y. Xue, B. Huang, H. Yu, C. Zhang, D. Zhang, D. Jia, Y. Zhao, Y. Li, H. Liu, Y. Li, *Nat. Commun.* **2018**, *9*, 5309; b) Y. Xue, Y. Guo, Y. Yi, Y. Li, H. Liu, D. Li, W. Yang, Y. Li, *Nano Energy* **2016**, *30*, 858 – 866.

[14] a) C. Wang, H. Yang, Y. Zhang, Q. Wang, *Angew. Chem. Int. Ed.* **2019**, *58*, 6099 – 6103; *Angew. Chem.* **2019**, *131*, 6160 – 6164; b) J. Deng, P. Ren, D. Deng, X. Bao, *Angew. Chem. Int. Ed.* **2015**, *54*, 2100 – 2104; *Angew. Chem.* **2015**, *127*, 2128 – 2132.

[15] a) B. Cai, A. Eychmüller, *Adv. Mater.* **2019**, *31*, 1804881; b) G. Fu, X. Yan, Y. Chen, L. Xu, D. Sun, J. M. Lee, Y. Tang, *Adv. Mater.* **2018**, *30*, 1704609; c) T. V. Tam, S. G. Kang, M. H. Kim, S. G. Lee, S. H. Hur, J. S. Chung, W. M. Choi, *Adv. Energy Mater.* **2019**, *9*, 1900945; d) Y. Hou, Z. Wen, S. Cui, X. Feng, J. Chen, *Nano Lett.* **2016**, *16*, 2268 – 2277.

[16] a) L. Lai, J. R. Potts, D. Zhan, L. Wang, C. K. Poh, C. Tang, H. Gong, Z. Shen, J. Lin, R. S. Ruoff, *Energy Environ. Sci.* **2012**, *5*, 7936 – 7942; b) H. Wang, T. Maiyalagan, X. Wang, *ACS Catal.* **2012**, *2*, 781 – 794.

[17] Y. Okamoto, *Appl. Surf. Sci.* **2009**, *256*, 335 – 341.

[18] a) R. Lord, Jr., F. A. Miller, *J. Chem. Phys.* **1942**, *10*, 328 – 341; b) K. Zhang, K. Xie, K. Yuan, W. Lu, S. Hu, W. Wei, M. Bai, C. Shen, *J. Mater. Chem. A* **2017**, *5*, 7309 – 7315.

[19] a) H. Li, X. Su, C. Bai, Y. Xu, Z. Pei, S. Sun, *Sens. Actuators B* **2016**, *225*, 109 – 114; b) S. Nayak, L. Mohapatra, K. Parida, *J. Mater. Chem. A* **2015**, *3*, 18622 – 18635.

[20] Y. Zhao, J. Liu, Y. Hu, H. Cheng, C. Hu, C. Jiang, L. Jiang, A. Cao, L. Qu, *Adv. Mater.* **2013**, *25*, 591 – 595.

[21] Z.-H. Sheng, L. Shao, J.-J. Chen, W.-J. Bao, F.-B. Wang, X.-H. Xia, *ACS Nano* **2011**, *5*, 4350 – 4358.

[22] J. Sun, S. E. Lowe, L. Zhang, Y. Wang, K. Pang, Y. Wang, Y. Zhong, P. Liu, K. Zhao, Z. Tang, *Angew. Chem. Int. Ed.* **2018**, *57*, 16511 – 16515; *Angew. Chem.* **2018**, *130*, 16749 – 16753.

[23] a) H. Zou, G. Li, L. Duan, Z. Kou, J. Wang, *Appl. Catal. B* **2019**, *259*, 118100; b) Y. Jia, L. Zhang, A. Du, G. Gao, J. Chen, X. Yan, C. L. Brown, X. Yao, *Adv. Mater.* **2016**, *28*, 9532 – 9538.

[24] L. Zhuang, Y. Jia, H. Liu, X. Wang, R. K. Hocking, H. Liu, J. Chen, L. Ge, L. Zhang, M. Li, *Adv. Mater.* **2019**, *31*, 1805581.

[25] a) F. Lima, J. Zhang, M. Shao, K. Sasaki, M. Vukmirovic, E. Ticianelli, R. Adzic, *J. Phys. Chem. C* **2007**, *111*, 404 – 410; b) T. H. Yu, T. Hofmann, Y. Sha, B. V. Merinov, D. J. Myers, C. Heske, W. A. Goddard III, *J. Phys. Chem. C* **2013**, *117*, 26598 – 26607; c) Y. Zheng, Y. Jiao, M. Jaroniec, S. Z. Qiao, *Angew. Chem. Int. Ed.* **2015**, *54*, 52 – 65; *Angew. Chem.* **2015**, *127*, 52 – 66; d) Z. Chen, Y. Song, J. Cai, X. Zheng, D. Han, Y. Wu, Y. Zang, S. Niu, Y. Liu, J. Zhu, X. Liu, G. Wang, *Angew. Chem. Int. Ed.* **2018**, *57*, 5076 – 5080; *Angew. Chem.* **2018**, *130*, 5170 – 5174.

[26] J. Huang, J. Han, R. Wang, Y. Zhang, X. Wang, X. Zhang, Z. Zhang, Y. Zhang, B. Song, S. Jin, *ACS Energy Lett.* **2018**, *3*, 1698 – 1707.

[27] J. Wang, L. Li, Z.-D. Wei, *Acta Phys. Chim. Sin.* **2016**, *32*, 321 – 328.

[28] Y. Gu, S. Chen, J. Ren, Y. A. Jia, C. Chen, S. Komarneni, D. Yang, X. Yao, *ACS Nano* **2018**, *12*, 245 – 253.

[29] F. Li, G.-F. Han, H.-J. Noh, J.-P. Jeon, I. Ahmad, S. Chen, C. Yang, Y. Bu, Z. Fu, Y. Lu, J.-B. Baek, *Nat. Commun.* **2019**, *10*, 4060.

Manuscript received: October 16, 2019

Accepted manuscript online: January 5, 2020

Version of record online: February 19, 2020